# Topology of Reverse Von-Kármán Vortex Street in the Wake of a Swimming Whale Shark

Arash Taheri

***Abstract***—In this paper, effects of the ventral body planform of a swimming whale shark on the formation of 'reverse von-Kármán vortex street' behind the aquatic animal are studied using Fluid-Structure Interaction (FSI) approach. In this regard, incompressible Navier-Stokes equations around the whale shark's body with a prescribed deflection dynamics are solved with the aid of Boundary Data Immersion Method (BDIM) and Implicit Large Eddy Simulation (ILES) turbulence treatment by WaterLily.jl solver; fully-written in Julia programming language. The whale shark flow simulations here are performed at high Reynolds number, i.e. $1.4 \times 10^7$ corresponding to the swimming of a 10 meter-whale shark at an average speed of 5 km/h. For comparison purposes, vortical flow generation behind a silky shark with a streamlined forehead eidonomy is also simulated at high Reynolds number, Re = $2 \times 10^6$, corresponding to the swimming of a 2 meter-silky shark at an average speed of 3.6 km/h. The results depict formation of distinct wake topologies behind the swimming sharks depending on the travelling wave oscillating amplitudes.

***Keywords***—Whale shark, vortex street, BDIM, FSI, functional eidonomy, bionics.

## I. INTRODUCTION

NON-LINEAR interplay between deflection dynamics of the aquatic animal's body and external morphology or eidonomy of the animal with the aquatic environment governs formation and ejection of vortices in the reverse von-Kármán vortex street behind the swimming animals [1]. In general, flexibility and bending of the aquatic animal's body affect 'vortex formation' process [1] and thrust production efficiency of natural propulsors [2]. In fact, all different types of inertial-aquatic swimmers adopt 'vortex generation' mechanisms for propulsion in the aquatic environment, including: anguilliform [3], [4], carangiform [3], [5], ostraciiform and also thunniform [6]. To investigate the effects of body deflection dynamics and animal's eidonomy on the aquatic locomotion, Computational Fluid Dynamics (CFD) can be utilized as a numerical 'test rig' without known limitations of the experimental techniques [3]-[20]. As can be found in the literature, Immersed Boundary Method (IBM) is one of the well-fitted techniques for these kinds of aquatic flow applications, such as anguilliform and carangiform swimming [3], [4], nematode-like locomotion [13]-[15] and jellyfish swimming [16], [17], to name a few.

In general, eidonomy of aquatic swimming animals plays a crucial role in onset and development of fluid flow phenomena involved in the animal's locomotion, such as: boundary layers, shear layers, flow detachments and reattachments, low/high speed regions on the body and vortices induced by the body deflection dynamics. There are several examples showing the importance of eidonomic features in swimming performance and locomotion of the aquatic animals [7]-[12]. For instance, eidonomic ventral pleats covering belly skin-surface of the humpback whales, *Megaptera novaeangliae*, generate low-speed strips and shear layer/vortex in the grooves. Formation of these low-speed regions can be directly translated to a relatively higher pressure region on the belly according to the Bernoulli equation. Therefore, it contributes to the buoyancy of the animal and lift generation [7]. In addition, the external morphology of the humpback whale's flipper contributes to stall delay and provides a flatter or softer behavior in the post-stall region [8]. In another example of the effects of external morphology of the aquatic animals, it was shown that the special external morphology or eidonomy of the cephalofoil tip of a scalloped hammerhead shark, *Sphyrna Lewini*, generates a tip vortex with a lower strength. In other words, hammerhead shark's cephalofoil tips in the eye-bulb region behave as a winglet over a wide range of angles of attack [9].

Whale sharks, *Rhincodon typus*, are charismatic swimmers as the largest fish on the earth, live in warm and tropical waters of oceans, seas and gulfs, such as Persian Gulf at the south of Iran. Their maximum size can reach 17-21.4 meters [21], [22]. One of the most important eidonomic features of a whale shark is the presence of prominent longitudinal ridges, which covers the dorsal and lateral parts of the whale shark's body (Fig. 1). As shown in the previous work [10], presence of these prominent ridges on the dorsal area of the whale shark's body leads to the formation of streamwise vortices in the skin-surface flow channels. It delays flow separation on the shark's body and furthermore modifies hydrodynamic characteristics of the whale shark's swimming including the vortical energy contents. The simulation results showed that for both streamwise swimming and locomotion with angles of attack or sideslip angles, streamwise vortices are generated in the skin-surface flow channels on the whale shark's body (Figs. 1 (a) and (b)). For instance, as one can see in Fig. 1 (b), streamwise vortex filaments are generated in the flow channels at an angle of attack, i.e. -30°, which follow external curvature of the body extending to the caudal fin. In the aforementioned study [10], as the first attempt to simulate turbulent flow fields over a whale shark, tail beating with a frequency (equals to $\omega$) was initially modeled by considering a linear inflow distribution over the tail-peduncle with a rigid body (no undulation) (Fig. 2 (a)) [10]. The turbulent flow simulations were all performed at a high Reynolds number,

A. Taheri, Ph.D., Mech. Eng., is with Division of Applied Computational Fluid Dynamics, Biomimetic and Bionic Design Group, Tehran, Iran (e-mail: taha.bionics @gmail.com).

World Academy of Science, Engineering and Technology
International Journal of Mechanical and Mechatronics Engineering
Vol:17, No:8, 2023

i.e. $1.4 \times 10^7$, with the aid of finite volume technique using Lam-Bremhorst turbulence treatment method. The simulation results clarified that if passing flows over the shark's body involve a lateral component of velocity (e.g. in swimming with sideslip angles or in the case of tail beating), a noticeable downward force is produced by the ridges, which contributes to what is so-called 'sinking feeling' for the sharks.
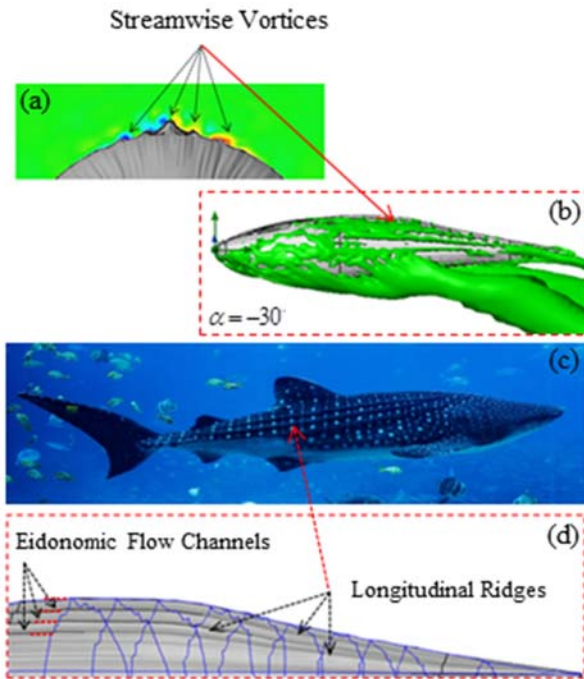


Fig. 1 Streamwise vortex generation in the skin-surface flow channels of a whale shark: (a) & (b) streamwise vortices, captured by $\lambda_2 = -10^5$ [10], (c) whale shark swimming (modified from original photo [23]), (d) 3D whale shark eidonomy model utilized for CFD simulations [10]

Physically, the prominent ridges disturb flows passing over the shark's body and reduces local velocity effectively, which in turn increase the pressure level on the dorsal zone of the animal's body compared to the ventral region according to the Bernoulli equation (Fig. 2 (b)). As a result, a downward force, opposite to the buoyancy, is generated. As one can also see in Fig. 2 (c) in the top view of the tail peduncle with/without ridges, a peak velocity zone with blue color (marked by the red-dashed oval in the left) is effectively omitted with the presence of the ridges; therefore, pressure increases on the top compared to the case without ridges. This explains how the extra downward force is majorly generated by the ridges. Flow pathlines, vortex formation patterns and the energy content of vortices are also modified by the longitudinal ridges [10].

In the present paper, another important eidonomic factor contributing in vortex formation characteristics behind a swimming whale shark is considered. Here, effects of the ventral body planform of whale sharks on the topology of the ejected vortices by the animal's body undulations are studied with the BDIM [24]-[30]. The results materialize wake patterns behind the swimming animal as a function of

travelling wave oscillating amplitudes. Details are presented in the following sections.
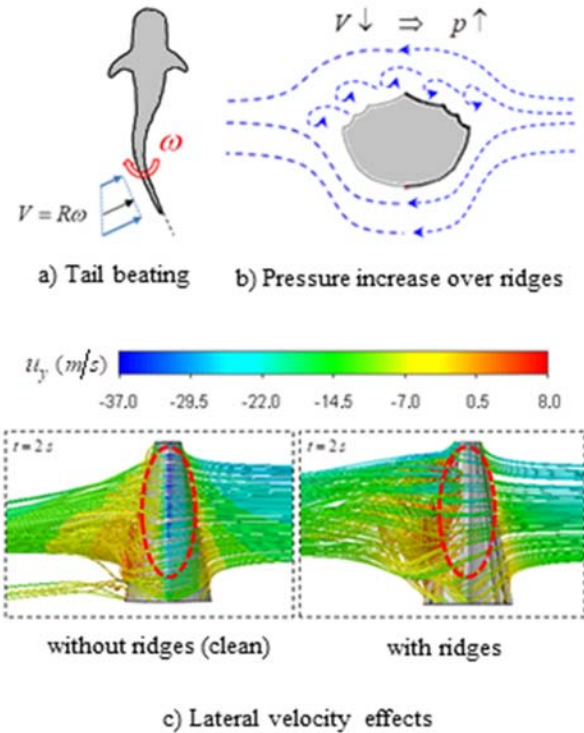


Fig. 2 Effects of ridges on passing flows with lateral component of velocity: (a) whale shark tail beating model, (b) schematic of pressure increase over the ridges due to the lateral velocity, (c) distribution of lateral velocity and pathlines in tail beatings with/without ridges [10]

## II. NUMERICAL METHODOLOGY

In general, to simulate wake flows induced by the repetitive body deflections of aquatic swimming animals, adopting CFD techniques like IBM [24] and BDIM [25]-[30] is very fruitful. In fact, these techniques are capable to efficiently simulate flow fields embracing deformable/dynamic objects in FSI problems. In these methods, incompressible Navier-Stokes equations governing the fluid domain ($\Omega_f$) can be formulated by the following equations:

$$\rho \left( \frac{\partial u_i(\vec{x},t)}{\partial t} + u_j(\vec{x},t) \cdot \frac{\partial u_i(\vec{x},t)}{\partial x_j} \right) \qquad \vec{x} \in \Omega_f \qquad (1)$$

$$= -\frac{\partial p(\vec{x},t)}{\partial x_i} + \mu \frac{\partial^2 u_i(\vec{x},t)}{\partial x_j \partial x_j}$$

$$\frac{\partial u_i(\vec{x},t)}{\partial x_i} = 0 \qquad \vec{x} \in \Omega_f \qquad (2)$$

For the deformable body domain ($\Omega_b$) or shark's body, the governing equation can be written as [28]:

$$u_i(\vec{x},t) = V_i^b(\vec{x},t) \qquad \vec{x} \in \Omega_b \qquad (3)$$

World Academy of Science, Engineering and Technology
International Journal of Mechanical and Mechatronics Engineering
Vol:17, No:8, 2023

where $\rho$ and $\mu$ are fluid density and viscosity, respectively. $V_i^b$ is the prescribed velocity for the immersed body [25]-[29]. To solve the above equations in the present paper, WaterLily.jl solver based on BDIM is utilized. The code is fully-written in Julia programming language, capable to be executed in parallel on computing systems with multi-threaded CPU and GPU architectures. Julia is an easy-to-use, general-purpose, high-performance and open-source programming language, which looks like Python and runs as fast and efficient as C and FORTRAN. It is also possible 'calling' libraries/codes, already written in C and FORTRAN in Julia, which makes it very attractive for CFD applications. Julia ecosystem includes several packages, such as [31]: scientific and quantum computing, data science, parallel computing, machine learning (ML) and visualization [32], to name a few.

WaterLily.jl solves fluid flow governing equations on a uniform Cartesian grid with BDIM [27]. The code provides an automatic differentiation to embed the deformable body into the flow field by a singled-distance function (*sdf*) and a mapping function. In the solution procedure, the solver adopts a 3$^{rd}$-order finite volume scheme [25] along with a data-driven geometric multigrid technique based on the ML concept for pressure projection step to boost-up the computations [30]. For high-Reynolds number turbulent flow simulations, e.g. flow simulations over sharks and whales, turbulence is also treated with the ILES method [25]. The utilized pre- and post-processing tools along with the 'WaterLily.jl' solver have been developed in Julia programming language for flow simulation applications, such as: external flows, flapping foils and fish swimming by Weymouth et al. [25], [26].

### III. GEOMETRY, DYNAMICS AND SIMULATION SETTINGS

To capture vortical structures in the wakes of swimming sharks/whales, the body geometry and its deflection dynamics should be pre-modeled. In general, there is a fundamental difference between the posture and motion of flukes in sharks and in whales and dolphins, due to evolution process over the course of millions of years. In fact, whales possess horizontal flukes, which move up and down in a vertical direction. It is believed that they have been evolved from their land-dwelling four-legged ancestors (mammals), lived about 50 million years ago. That's why their backbones naturally tend to bend up and down, not from side to side like fishes. Furthermore, it seems that this horizontal tail configuration can efficiently produce enough propulsion to break the water surface for breathing of these breath-hold aquatic animals. On contrast, sharks are fish and their fluke is positioned vertical and moves from side to side for bio-propulsion generation. Therefore, for 2D flow simulations of the induced reverse von-Kármán vortex street behind sharks, ventral (bottom) planforms should be modeled, while for whales and dolphins, the side-view planform of the animal's body should be constructed for computations.

#### A. Shark's Ventral Planform

In general, whale sharks exhibit a streamlined body with a semi-blunt forehead and have dorsal, pectoral, pelvic, anal and caudal fins, as shown in Fig. 3. To construct whale shark's ventral planform, here eleven control points are adopted to accurately define the body's boundary edge (Fig. 3). Then the planform is constructed with fitting of a spline curve through the control points [26]. As mentioned before, there are several prominent longitudinal ridges covering the dorsal and lateral regions of the whale shark's skin, which have no contribution into the ventral planform layout, as one can see in Fig. 3.
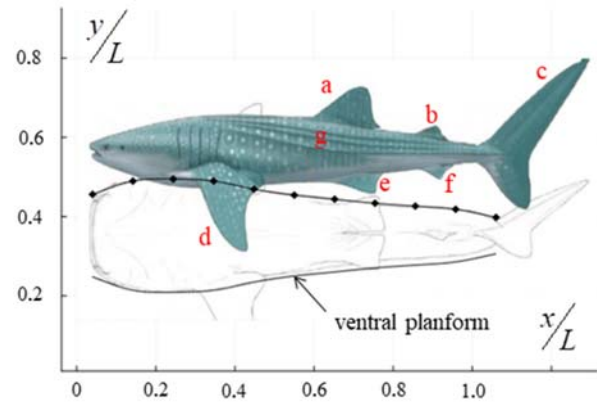


Fig. 3 Whale shark ventral planform model (black curve-spline); shark's eidonomy: a. 1$^{st}$ dorsal fin, b. 2$^{nd}$ dorsal fin, c. caudal fin, d. pectoral fin, e. pelvic fin, f. anal fin, g. longitudinal ridges (modified from the original photo of a whale shark [33])

In this paper, wake flows behind a swimming silky shark with a narrower streamlined body are also considered for comparison purposes. Fig. 4 depicts curve-fitting applied for construction of the ventral planform layout. As shown in the figure, the forehead region of the planform is thinner in this case and forms a well-fitted 'bullet-type' or streamlined body compared to the whale shark's planform (Fig. 3). Like whale sharks, silky sharks also have dorsal, pectoral, pelvic, anal and caudal fins, as shown in Fig. 4.
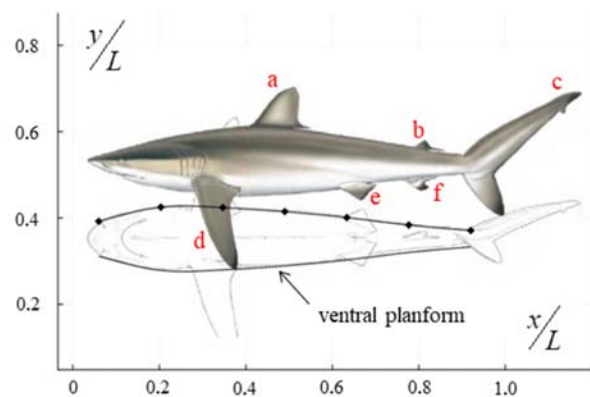


Fig. 4 Silky shark ventral planform model (black curve-spline); shark's eidonomy: a. 1$^{st}$ dorsal fin, b. 2$^{nd}$ dorsal fin, c. caudal fin, d. pectoral fin, e. pelvic fin, f. anal fin (modified from the original photo of a silky shark [33])

#### B. Shark's Body Deflection Dynamics

After defining the planform layout, the next step is to apply deflection dynamics to the model. In this regard, deformable

World Academy of Science, Engineering and Technology
International Journal of Mechanical and Mechatronics Engineering
Vol:17, No:8, 2023

slender body approach, proposed by Lighthill, can be utilized [34]. In the procedure [26], travelling wave concept is applied to describe backbone (body centerline) dynamics of the fish (i.e. planform). The backbone (body centerline) dynamics can be explicitly defined with an undulatory (sinus) function with variable amplitudes in the longitudinal direction, as:

$$y = A_\xi \xi(x) \qquad (4)$$

$$\xi(x) = A_c(x)\sin(kx - 2\pi ft) \qquad (5)$$

where $A_\xi$ is the oscillation amplitude per body length. $\xi(x)$ is the normalized travelling wave amplitude, plotted in $0 < t < 1$ for $k = 4.5$ and $f = 1$ in Fig. 5. $A_c(x)$ also defines boundaries of the oscillating amplitude envelope by control points (e.g. 6 control points in Fig. 5, marked by the black diamond) and $k$ is wave number of the travelling wave. $f$ is the undulation frequency and is defined by:

$$f = St(U / 2A_\xi) \qquad (6)$$

where $St$ is the Strouhal number, defined as $St = \omega A_\xi / U$. Furthermore, $U$ and $L$ is considered as characteristic velocity and body length, respectively. Angular velocity is also defined as $\omega = 2\pi f$. As one can see in Fig. 5, deflection dynamics envelope consists of two intervals: first, head-yawing interval, mimicking shark's head moving from left to right vice-versa with low-amplitude; second, body-tail oscillation interval with relatively larger amplitudes, responsible for the animal's bio-propulsion generation mechanism.
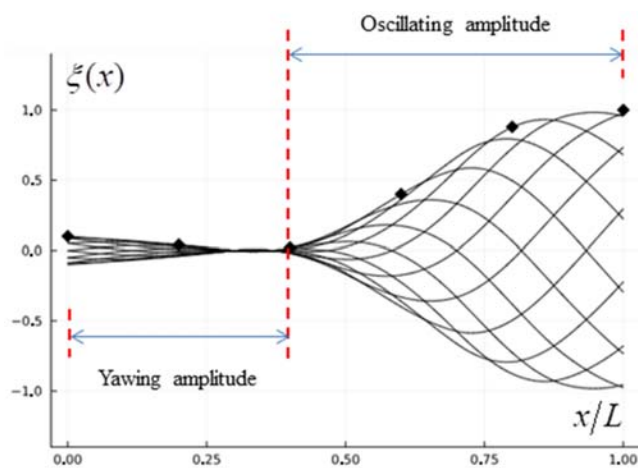


Fig. 5 Normalized traveling wave amplitude, describing body deflection dynamics, including: head-yawing interval ($0 < x / L < 0.4$) and body-tail oscillation interval ($0.4 < x / L < 1.0$)

*C. Flow Simulation Settings*

Whale shark wake flow simulations here are performed at a high Reynolds number, $Re = UL / \upsilon = 1.4 \times 10^7$; where $\upsilon$ is the kinematic viscosity. It corresponds to the swimming of a 10 meter-whale shark at an average speed of 5 km/h. Silky shark wake flows are also simulated at high Reynolds number, $2 \times 10^6$, corresponding to the swimming of a silky shark with a body length of 2 meters at an average speed of 3.6 km/h.

As observed by Gazzola et al. [35], based on more than one thousand measurements on the swimming and flying species in the inertial range, for turbulent flows at high Re numbers, i.e. $Re > 3 \times 10^3$, or equivalently at high swimming number $Sw = \omega A_\xi L / \upsilon > 10^4$, Strouhal number is constant ($St \approx 0.3$) and is independent of $Re$ and $Sw$. Therefore, for whale shark and silky shark simulations here, $St = 0.3$ is applied. In the present study, swimming number $Sw$ is equal to $6.67 \times 10^6$ and $4.67 \times 10^7$ for the silky and whale sharks, respectively; as implemented by $Sw = Re \times St$ [35]. As mentioned before, to simulate turbulent flows over the sharks, an ILES method is hired using the WaterLily.jl solver [25]. A computational domain equals to (6L, 2L) and a total time of 20 s is considered for all simulations here, as a compromise between the computational efforts and boundary/transient effects. The size of the domain enables to capture vortical dynamics and the reverse von-Kármán vortex street behind the aquatic animal in full. A uniform grid with a resolution equal to 1152 $\times 384$ is adopted in x and y directions, respectively. All parallel flow numerical simulations are performed on NVIDIA 930M GPU with 384 CUDA cores with about 1GHz speed.

## IV. RESULTS AND DISCUSSION

In this section, wake patterns formed behind a swimming whale shark are presented. As mentioned before, wake flows behind a swimming silky shark are also captured by the numerical simulations for comparison, which provide a better insight into the underlying physics of the problem. Fig. 6 depicts vortex formation phenomena in the reverse von-Kármán vortex street behind a silky shark with a bullet-type streamlined body at the different oscillation amplitudes ($A_\xi$).

To illustrate vortices in this paper, contours of the normalized vorticity, $\omega_z^\dagger$ defined by $\omega_z^\dagger = \omega_z U / L$ are shown. As one can see in Fig. 6 (d), for the lowest oscillation amplitude here, i.e. $A_\xi = 0.1$, boundary layers with the opposite vorticity signs develop on the different sides of the body and remain attached up to the tail. At the tail's utmost end, boundary layers roll up by the shark's tail deflection dynamics and form an entity called a 'vortex'. The vortex is then ejected into the wake flow behind the swimming shark. By continuous repetitive shark's tail beatings, these vortices with opposite vorticity signs are continuously formed, ejected and washed out downstream. These ejected vortices interact with each other in the wake flows, while transporting towards the downstream. These nonlinear phenomena make an interesting pattern, called 'reverse von-Kármán vortex street' behind the swimming aquatic animals. For this low oscillation amplitude, $A_\xi = 0.1$, overall the 'vortex envelope' is bounded and almost limited between two parallel horizontal lines (Fig. 6 (d)). By increasing the oscillation amplitude to $A_\xi = 0.15$ (Fig. 6 (c)), some kinds of instabilities develop in the boundary layers,

World Academy of Science, Engineering and Technology
International Journal of Mechanical and Mechatronics Engineering
Vol:17, No:8, 2023

somewhere around the middle section of the shark's body (instability onset). As shown in the figure, von-Kármán street also expands in the lateral direction and the vortices get farther from each other. Hence, a more complex vortex distribution pattern is obtained due to the chaotic dynamics of the vortex interactions, induced by the larger oscillation amplitude.
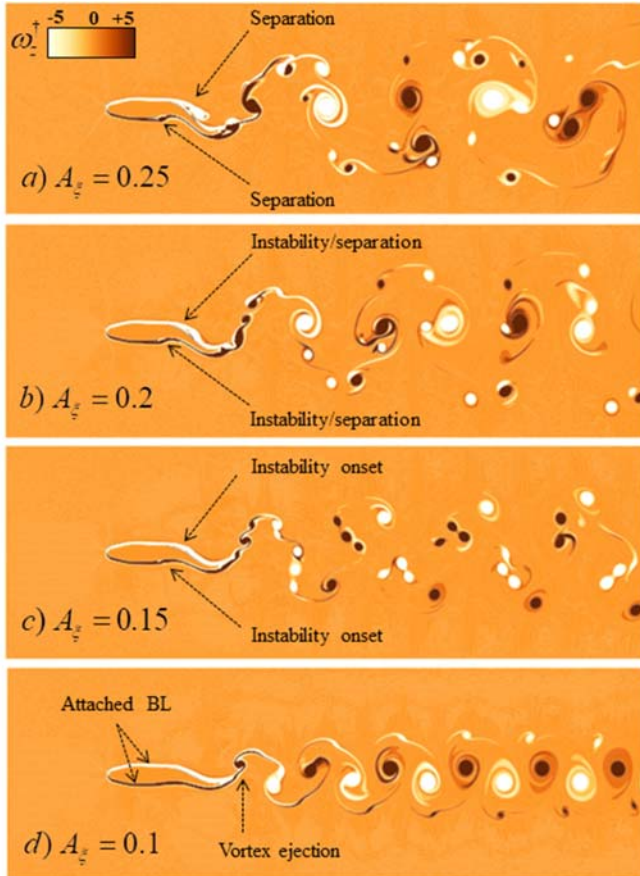


Fig. 6 Topology of vortices in the reverse von-Kármán vortex street behind a *silky shark* at different oscillation amplitudes: a) $A_\xi = 0.25$,

b) $A_\xi = 0.2$, c) $A_\xi = 0.15$, d) $A_\xi = 0.1$

Fig. 7 explains development of the boundary layers with opposite vorticity signs on different sides of the shark's body including $\omega_z > 0$ and $\omega_z < 0$ regions using the slender body theory, as observed for silky and whale sharks in Figs. 6 and 8. As observed in Fig. 6 (b), for the oscillation amplitude equals to 0.2, more pronounced vortices are generated by tail-body undulations and instability/separation gradually grows on the shark's body. Ultimately, by increasing the oscillation amplitude to 0.25 in Fig. 6 (a), separation occurs on the silky shark's body, which leads to an energy loss for the fluid flow system in the shark's swimming process.

In general, the most efficient swimming happens at $A_\xi = 0.1$ for the silky shark among all other cases, when vortices are exclusively ejected from the tail with no flow separation occurrence on the body. When instability starts to develop and separation happens on the body, energy loss occurs, as also

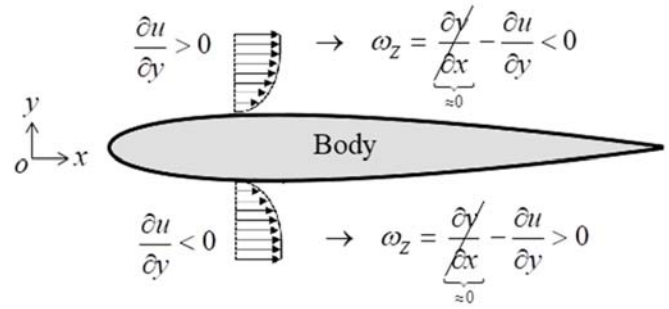observed for a dogfish shark by Weymouth [26].



Fig. 7 Schematics of 2D boundary layer development on the aquatic animal's body and its corresponding vorticity ($\omega_z$) sign
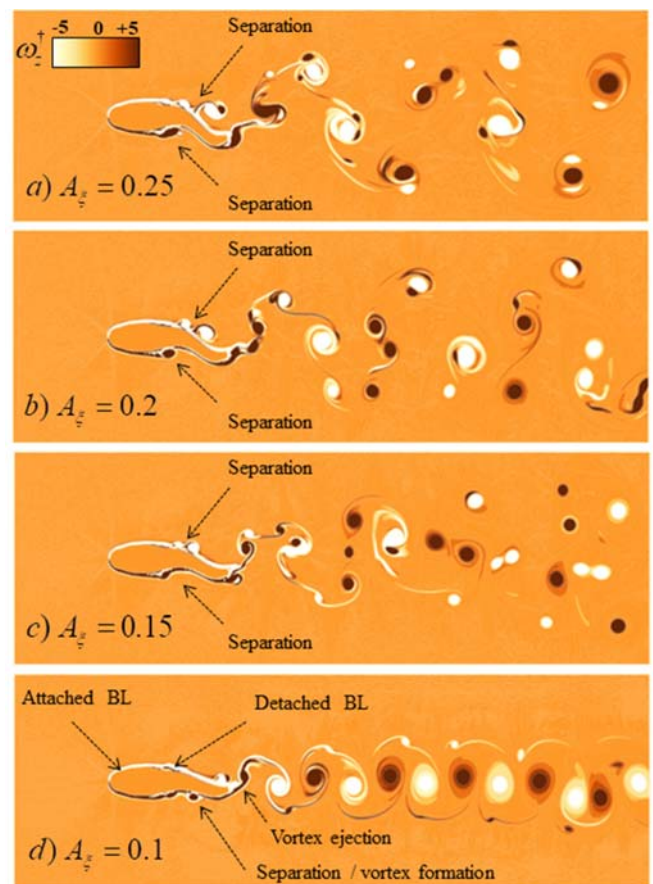


Fig. 8 Topology of vortices in the reverse von-Kármán vortex street behind a *whale shark* at different oscillation amplitudes: a) $A_\xi = 0.25$, b) $A_\xi = 0.2$, c) $A_\xi = 0.15$, d) $A_\xi = 0.1$

Fig. 8 illustrates formation of 'reverse von-Kármán vortex street' behind a swimming whale shark. As one can see in the figure, for all the oscillation amplitudes from 0.1 to 0.25, separation occurs on the body, even at $A_\xi = 0.1$. In fact, as mentioned before, the 2D ventral planform of a whale shark possesses a semi-blunt forehead (Fig. 3), which triggers flow separation over the body and leads to an energy loss for the shark's fluid flow system. As shown in Figs. 8 (a)-(d),

World Academy of Science, Engineering and Technology
International Journal of Mechanical and Mechatronics Engineering
Vol:17, No:8, 2023

boundary layer flow is initially attached and then becomes detached at the middle section in the body convergence region ($x/L > 0.3$) with a negative curve slope ($dy/dx < 0$) and an adverse pressure gradient ($\partial p / \partial x > 0$), as observed in Fig. 3. In other words, whale shark's body is thick at forehead region compared to the silky shark's body; this can be directly translated to a higher unfavorable adverse pressure gradient, which in turn increases tendency of the flow separation for the whale shark. As one can also see in Fig. 8 (d), for $A_\xi = 0.1$ vortices are formed by the repetitive tail beatings or deflection dynamics and then continuously ejected into the downstream flow behind the animal, similar to the silky shark (Fig. 6 (d)). Although the relative sizes of the vortices generated by the thicker whale shark's body are bigger than the vortices produced in the silky shark swimming process, by increasing the oscillation amplitude from 0.1 to 0.25, as shown in Fig. 8, 'reverse von-Kármán vortex street' envelope expands in the lateral direction and nonlinear dynamics of the vortices become more chaotic, having a high level of interactions between the vortices. As a result, by increasing the oscillation amplitudes, 'reverse von-Kármán vortex street' pattern of a whale shark becomes more and more complicated (Fig. 8).
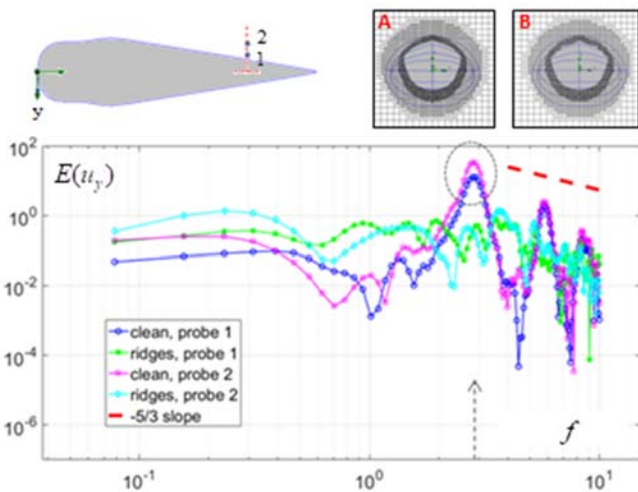


Fig. 9 Effects of ridges on the energy content of vortical structures in flow passing over the whale shark's peduncle with lateral component of velocity, typically generated in the tail beating process; Probe positions: 1 and 2 (top-left) in the peduncle region, whale shark body without ridges (A) and with ridges (B) (top-right), energy content of the lateral velocity signal vs. frequency captured at two probe points for the whale shark with/without longitudinal ridges (bottom) [10]

It is worth re-mentioning that occurrence of flow separation over the whale shark's body, as observed in Fig. 8, leads to energy loss for the swimming process. In fact, presence of the prominent longitudinal ridges on the whale shark's dorsal and lateral sections of the body also modifies formation, evolution and ejection of the vortices and separation onset and dynamics in 3D, which is not present by the adopted flow simulation strategy using a 2D ventral planform here. As shown in the previous work by unsteady flow simulations over the whale shark's peduncle with/without ridges [10], presence of the

ridges radically modify evolution of separated vortical flows on the shark's body (Fig. 2 (c)). It also makes energy content of the vortical structures originating from the peduncle more uniform via suppressing overshoot/undershoot peaks (Fig. 9). In these simulations as mentioned before, whale shark's body was considered rigid (without any body deflection) and tail beating was implemented by a linear inflow (Fig. 2 (a)) [10].

Furthermore, in 3D flow simulations, having another degree of freedom compared to the 2D flow simulations, provides a larger room for the passing flows over the whale shark to embrace the streamlined forehead section, which in turn can minimize flow separations. In addition, skin-surface channels formed by the longitudinal ridges generate streamwise vortices and guide the passing flows around the forehead section in a way to minimize the separation [10]. Therefore, it seems that separation occurrence captured in the 2D flow simulations on the whale shark's body will be more limited in 3D.

## V. CONCLUSION

In this paper, wake flow patterns behind a swimming whale shark were obtained at high Reynolds number for different values of the oscillation amplitudes. In addition, reverse von-Kármán vortex street generated behind a silky shark having a narrower body was also captured by numerical simulations for comparison purposes. In the adopted numerical methodology, effects of the ventral planform on the reverse von-Kármán vortex street were considered. The simulation results depict formation, ejection and transportation of vortices originating from the whale shark's body-tail into the downstream flows. For silky sharks, separation on the body gradually develops by increasing the oscillation amplitude parameter. For whale sharks with a thicker body, possessing a semi-blunt forehead, separation occurs for all values of the oscillation amplitudes. For both sharks, propulsive vortices are repetitively generated by the tail with opposite vorticity signs and released into the downstream flow. Although size of the vortices is relatively bigger for a whale shark with a thicker ventral body planform compared to a silky shark. As demonstrated by the simulation results here, pattern and dynamics of the ejected vortices in the wake of both sharks become more chaotic and complicated by increasing the oscillation amplitude. According to the results of the 3D numerical flow simulations over a whale shark with a rigid body (without any deflection), it seems that separation occurrence on the body will be more limited in 3D; due to having an extra degree of freedom compared to 2D and also presence of the longitudinal ridges forming skin-surface flow channels on the whale shark's body. Overall, the present work identified vortical structures behind a swimming whale shark by considering a 2D ventral planform of the shark's body. As future work, to capture a more complete 3D pattern of the vortices and grasp a deeper understanding about the evolution of the vortices, 3D flow generated by the swimming shark should be simulated by considering a deformable 3D model of a whale shark with the prominent longitudinal ridges. In this regard, applying the IBM along with a wall-modeled LES turbulence treatment will be fruitful.

## Acknowledgment

## References

[1] A. Taheri, *Fluid Dynamics and Bio-Propulsion of Animal Swimming in Nature (Bionics)*. 1st ed., Tehran: Arshadan Publication, 20 Chapters, 692 pages, 2021.

[2] K.N. Lucas, N. Johnson, W.T. Beaulieu, E. Cathcart, G. Tirrell, S.P. Colin, B.J. Gemmell, J.O. Dabiri, and J.H. Costello, "Bending rules for animal propulsion", *Journal of Nature Communications*, vol.5, no.3293, pp.1-7, DOI: 10.1038/ncomms4293, 2014.

[3] I. Borazjani, "Numerical simulations of fluid-structure interaction problems in biological flows", Ph.D. thesis, Department of Mechanical Engineering, *University of Minnesota*, 2008.

[4] M.S.U. Khalid, J. Wang, I. Akhtare, H. Dong, M. Liu and A. Hemmati, "Why do anguilliform swimmers perform undulation with wavelengths shorter than their bodylengths?", *Physics of Fluids*, vol.33, no.3, 031911, DOI:10.1063/5.0040473, 2021.

[5] A.P. Maertens, A. Gao and M.S. Triantafyllou, "Optimal undulatory swimming for a single fish-like body and for a pair of interacting swimmers", *Journal of Fluid Mechanics*, vol.813, pp.301-345, 2017.

[6] N. Li, H. Liu and Y. Su, "Numerical study on the hydrodynamics of thunniform bio-inspired swimming under self-propulsion", *PLoS ONE*, vol.12, no.3, 2017.

[7] A. Taheri, "On the hydrodynamic effects of humpback whale's ventral pleats", *American Journal of Fluid Dynamics*, vol.8, no.2, pp.47-62, 2018.

[8] A. Taheri, "A meta-model for tubercle design of wing planforms inspired by humpback whale flippers", *International Journal of Aerospace and Mechanical Engineering*, vol.12, no.3, pp.315-328, 2018.

[9] A. Taheri, "On the hydrodynamic effects of the eidonomy of the hammerhead shark's cephalofoil in the eye bulb region: Winglet-like behaviour", *International Journal of Marine Science and Technology Bulletin*, vol. 11, no.1, pp.41-51, 2022.

[10] A. Taheri, "Hydrodynamic impacts of prominent longitudinal ridges on the 'whale shark' swimming", *Research in Zoology*, 2020, vol.10, no.1, pp.18-30, 2020.

[11] A. Taheri, "Hydrodynamic analysis of bionic chimerical wing planforms inspired by manta ray eidonomy", *Indonesian Journal of Engineering and Science*, vol.2, no.3, pp.11-28, 2021.

[12] K. Bang, J. Kim, S.I. Lee and H. Choi, "Hydrodynamic role of longitudinal dorsal ridges in a leatherback turtle swimming", *Scientific Reports, Nature Journal*, vol.6, no. 34283, doi:10.1038/srep34283, 2016.

[13] A. Battista, "Swimming through parameter subspaces of a simple anguilliform swimmer", *Integrative and Comparative Biology*, vol.60, no.5, pp. 1221–1235, 2020.

[14] N.A. Battista, "Diving into a Simple Anguilliform Swimmer's Sensitivity", *Integrative and Comparative Biology*, vol.60, no.5, pp. 1236–1250, 2020.

[15] A. Taheri, "Lagrangian flow skeletons captured in the wake of a swimming nematode C. elegans using an immersed boundary fluid-structure interaction approach", *International Journal of Bioengineering and Life Sciences*, vol.15, no.7, pp.71-78, 2021.

[16] A. Taheri, "Lagrangian coherent structure analysis of jellyfish swimming using immersed boundary FSI simulations", *Journal of Mechanical and Civil Engineering*, vol.15, no.1, pp.69-74, 2018.

[17] J.G. Miles and N.A. Battista, "Naut your everyday jellyfish model: exploring how tentacles and oral arms impact locomotion", *Fluids*, vol.4, no.169, doi:10.3390/fluids4030169, 2019.

[18] N.A. Battista, A.J. Baird and L.A. Miller, "A mathematical model and MATLAB code for muscle-fluid-structure simulations", *Journal of Integrative and Comparative Biology*, vol.55, no.5, pp.901-911, 2015.

[19] N.A. Battista, W.C. Strickland, and L.A. Miller, "IB2d: a Python and MATLAB implementation of the immersed boundary method", *Bioinspiration and Biomimicry Journal*, vol.12, no.3, 036003, 2017.

[20] N.A. Battista, "Fluid-Structure Interaction for the Classroom: Interpolation, Hearts, and Swimming!", *SIAM Review*, vol.63, no.1, pp. 181-207, 2021.

[21] L. Copmpagno, M. Dando and S. Fowler, *Sharks of the world*. 1st ed., New Jersey: Princeton University Press, 368 pages, 2005.

[22] C.R. McClain, M.A. Balk, M.C. Benfield, T.A. Branch and C. Chen, "Sizing ocean giants: patterns of intraspecific size variation in marine megafauna", *PeerJ Journal*, doi:10.7717/peerj.715, 2015.

[23] Photo from P. Xu, Georgia Aquarium- Atlanta, www.unsplash.com.

[24] C.S. Peskin, "The immersed boundary method", *Acta Numerica Journal*, vol.11, pp.479-517, 2002.

[25] G.D. Weymouth and B. Font, "WaterLily.jl: A differentiable fluid simulator in Julia with fast heterogeneous execution", *34th International Conference on Parallel Computational Fluid Dynamics*, Cuenca, Ecuador, 29–31 May, 2023.

[26] G.D. Weymouth, "Simulation of a swimming dogfish shark", presented at *www.Julialang.org*, August 2021.

[27] G.D. Weymouth and D.K.P. Yue, "Boundary data immersion method for Cartesian-grid simulations of fluid-body interaction problems", *Journal of Computational Physics*, vol.230, pp.6233-6247, 2011.

[28] A.P. Maertens and G.D. Weymouth, "Accurate Cartesian-grid simulations of near-body flows at intermediate Reynolds numbers", *Computer Methods in Applied Mechanics and Engineering*, vol.283, pp.106-129, 2015.

[29] M. Lauber, G.D. Weymouth, and G. Limbert, "Immersed boundary simulations of flows driven by moving thin membranes", *Journal of Computational Physics*, p.111076, 2022.

[30] G.D. Weymouth, "Data-driven multi-grid solver for accelerated pressure projection", *Computers & Fluids*, vol.246, p.105620, 2022.

[31] www.Julialang.org.

[32] S. Danisch and J. Krumbiegel, "Makie.jl: Flexible high-performance data visualization for Julia", *Journal of Open Source Software*, vol.6, no.65, DOI:10.21105/joss.03349, 2021.

[33] D.A. Elbert, *On board guide for the identification of pelagic sharks and rays of the western Indian Ocean*, Illustrator: M. Dando, Food and Agriculture Organization of The United Nations, 2014.

[34] J. Lighthill, "Note on the swimming of slender fish", *Journal of Fluid Mechanics*, vol.9, no.2, pp.305 – 317, 1960.

[35] M. Gazzola, M. Argentina and L. Mahadevan, "Scaling macroscopic aquatic locomotion", *Nature Physics*, vol.10, pp.758-761, 2014.